Acta Mech
https://doi.org/10.1007/s00707-024-04206-4

ORIGINAL PAPER

Jack L. Eatson · Benjamin T. Stephenson · Jacob R. Gordon · Tommy S. Horozov · D. Martin A. Buzza

Capillary assembly of anisotropic nanoparticles at cylindrical fluid interfaces in the immersion regime

Received: 29 May 2024 / Revised: 22 November 2024 / Accepted: 17 December 2024

Abstract The unique behaviour of colloids at liquid interfaces provides exciting opportunities for engineering the assembly of colloidal particles into functional materials. In particular, the deformable nature of liquid interfaces means that we can use interfacial curvature, in addition to particle properties, to direct self-assembly. In this paper, we use a finite element method to study the self-assembly of rod-shaped particles adsorbed at a curved interface formed by a sessile drop with cylindrical geometry, where the lateral width of the cylindrical drop is much greater than the length of the rods, and the height of the drop is comparable to or smaller than the radius of the rods, i.e. the system is in the so-called immersion regime. Specifically, we study the configuration of single and multiple rods as a function of drop height, particle shape (ellipsoid, cylinder, spherocylinder) and contact angle. We find that for low enough drop heights, regardless of the shape or contact angle of the particles, all rods orientate themselves parallel to the long axis of the cylindrical interface and are strongly confined laterally to be at the centreline of the cylindrical drop. The rods also experience long-range immersion capillary forces which assemble the rods tip-to-tip at larger drop heights and, in the case of ellipsoids and spherocylinders, side-to-side at smaller drop heights. We note that the capillary forces that drive particle ordering are very strong in the immersion regime, even for rods on the nanoscale, allowing us to control the configuration of nanorods using near micron-scale droplets. Our capillary assembly method therefore provides a facile method for creating functional nanoclusters. Our study also provides insights into how the structure of such clusters evolves during the drying of the droplet.

1 Introduction

Colloidal particles adsorbed at liquid interfaces are of great importance for a wide range of applications including emulsification [1, 2], encapsulation [3], food and pharmaceuticals [4], reconfigurable biomimetic systems [5] and surface patterning [6, 7]. They also provide an ideal system for studying self-assembly due to a number of attractive features. For example, due to the very high detachment energies for typical particles [8], adsorbed colloids are highly confined to liquid interfaces, allowing us to study self-assembly in two dimensions [9, 10]. In addition, since liquid interfaces are soft, they are easily deformed by the adsorbed particles due to gravity, particle shape and protrusion of particles at a substrate, generating strong and long-ranged capillary

Supplementary Information The online version contains supplementary material available at https://doi.org/10.1007/s00707-024-04206-4..

J. L. Eatson · B. T. Stephenson · D. M. A. Buzza (✉)
Department of Physics & Mathematics, University of Hull, Hull HU6 7RX, UK
e-mail: d.m.buzza@hull.ac.uk

J. R. Gordon · T. S. Horozov
Department of Chemistry & Biochemistry, University of Hull, Hull HU6 7RX, UK

Published online: 09 January 2025

interactions between the particles [11–15]. These interactions provide a powerful handle with which to control and study self-assembly.

At a flat interface, when the height of the fluid subphase below the particle is greater than the size of the particle, we are in the so-called flotation regime [11, 12]. In the flotation regime, the solid substrate below the fluid subphase plays no role in determining the meniscus deformation around the adsorbed particle. In this case, for spherical particles with homogeneous surface chemistry, meniscus deformations can only arise due to gravity and the resultant meniscus deformations are circularly isotropic [16]. Exploiting the beautiful mathematical analogy between capillary forces and electrostatics, where positive and negative deformations of the interface are analogous to positive and negative 'charges', respectively, the capillary interactions between heavy spherical particles are therefore essentially monopolar in nature [11]. Such gravity-induced monopolar capillary interactions are generally only significant for large particles with sizes above 10 μm [2]. However, for particles with homogeneous surface chemistry but anisotropic shape such as ellipsoids or cylinders, capillary interactions can still be significant below this size. This is because to minimise interfacial energy, the liquid interface is required to meet the particle surface at a specific angle (known as the contact angle), and this constant contact angle requirement leads to quadrupolar meniscus deformations around the particle consisting of two rises and two falls in the contact line [17–19]. These undulations lead to orientationally dependent quadrupolar capillary interactions [18–20], driving ellipsoidal particles to assemble side-to-side [20–22] and cylindrical particles to assemble tip-to-tip [19, 22]. On the other hand, when the height of the fluid subphase is smaller than the size of the particle, we are in the so-called immersion regime [11, 12]. In this case, the height of the three-phase contact line on the particle is greater than the interface height, causing the particle to protrude above the fluid subphase, leading to strong monopolar deformations of the fluid interface [23]. These deformations lead to long-range monopolar interactions between particles that are significant down to the nanoscale [11, 15].

In the case of non-planar fluid interfaces, we can also use the curvature of the interface as an effective external field to direct self-assembly. For example, for spherical particles at a curved liquid interface, the deviatoric curvature of the interface induces quadrupolar capillary interactions between the particles and causes them to organise into regular square lattices [24]. Furthermore, if the spheres are adsorbed at a curved interface with non-uniform deviatoric curvature (e.g. a catenoid), they migrate to regions of high curvature to minimise the distortion to the interface [25, 26]. Not surprisingly, the effect of curvature is stronger for anisotropic rod-shaped particles which possess an intrinsic 'capillary quadrupole' due to undulations in their contact line. When such rods are adsorbed at a curved interface, the rods will rotate until their quadrupolar rise axis is aligned with the principal axis of curvature of the host interface where the interface is concave up [27, 28]. Indeed, Lewandowski et al. demonstrated that it is possible to suppress tip-to-tip assembly for two cylindrical particles in favour of side-to-side assembly when the cylinders are adsorbed at a curved interface where the energy penalty for the cylinders to reorientate to achieve the tip-to-tip configuration becomes prohibitive [28]. In addition, when rod-shaped particles are adsorbed at a liquid interface with non-uniform curvature, the particles will migrate towards regions of high deviatoric curvature and simultaneously align themselves along the principal axis of curvature of the host interface [29]. Interestingly, this physical phenomenon can be found in nature as some insects exploit this property for propulsion by deforming their bodies to create a capillary quadrupole that interacts with the curved menisci at the edge of a water surface [30, 31].

In a previous study, we explored the self-assembly of anisotropic rod-like particles at a curved interface formed by a cylindrical sessile drop, where the width of the drop was much larger than the length of the rods, and the height of the drop was much greater than the radius of the rods so that we are in the flotation regime [32]. The advantage of using a cylindrical drop is that the geometry of the curved interface is very simple (constant finite curvature transverse to the cylinder, zero curvature along the cylinder), allowing us to elucidate the interplay between interfacial curvature and particle properties in determining the behaviour of single and multiple rods. Using this curved geometry, we showed that it was possible to control the rods to align parallel, perpendicular or obliquely with respect to the long axis of the sessile drop by tuning the contact angle and particle shape. We also showed that the orientational confinement of the rods in the flotation regime was strong (e.g. orientational confining potential of 100 s of k_BT for nanoscale rods). However, we also found that the spatial confinement of the rods transverse to the long axis of the cylindrical drop and the capillary interaction between rods was much weaker compared to the orientational confinement (e.g. spatial confining potential and capillary interaction of 10 s of k_BT for nanoscale rods), limiting the degree to which we could align and assemble neighbouring particles into defined cluster structures in this regime.

To overcome these limitations, in this paper we study the self-assembly of rod-shaped particles at a cylindrical sessile drop in the immersion regime, i.e. where the height of the drop is comparable to or smaller

than the radius of the rods. Specifically, we use the finite element method Surface Evolver [33] to study the self-assembly of single and multiple rods as a function of drop height, particle shape (ellipsoid, cylinder, spherocylinder) and particle contact angle. As we will see later in the paper, although working in the immersion regime leads to slightly weaker orientational confinement of the rods due to a decrease in the curvature of the cylindrical interface, we can still achieve strong orientational confinement even for rods on the nanoscale. More importantly, we show that it is now possible to achieve very strong spatial confinement of the rods lateral to the cylindrical drop because the confining potential is a strong function of drop height in the immersion regime and drop height varies with lateral position. We also show that the capillary interactions between the rods in the immersion regime are much stronger and longer ranged because they are monopolar rather than quadrupolar in nature. Working in the immersion regime thus gives us good control over the orientation, position and self-assembly of rod-like particles adsorbed on a cylindrical drop, providing a facile method for creating to functional nanoclusters.

The rest of the paper is organised as follows. In Sect. 2, we describe the geometry and thermodynamics of the system as well as the finite element method (Surface Evolver) we use to study the system. In Sect. 3, we present and discuss results for the orientation and spatial confinement of single rods and the self-assembly of two rods at a cylindrical liquid drop as a function of drop height, particle shape and contact angle. Finally in Sect. 4, we present our conclusions.

2 Theoretical model

In this section, we discuss the geometry and thermodynamics of the system, which consists of rod-like particles adsorbed at a sessile cylindrical drop, as well as the Surface Evolver method we use to study this system theoretically.

For the rod-like particles, we consider particles with homogeneous surface chemistry with three particle shapes, i.e. ellipsoids, cylinders and spherocylinders (Fig. 1a). Note that for non-neutrally wetting rods (i.e. contact angle not equal to 90°) adsorbed at a flat interface, the constant contact angle requirement can be satisfied by a flat interface for spherocylinders but leads to quadrupolar meniscus deformations around ellipsoids and cylinders [17–19]. Ellipsoids and cylinders therefore possess an intrinsic capillary quadrupole, while spherocylinders do not [32]. For ellipsoids and cylinders, we use the super-ellipsoid equation [22, 34].

$$f\left(x', y', z'\right) = 1 \tag{1}$$

where

$$f\left(x', y', z'\right) = \left(\frac{x'^2}{a^2}\right) + \left(\frac{y'^2 + z'^2}{b^2}\right)^{\eta} \tag{2}$$

to define the particle shape, where x', y', z' are the Cartesian coordinates in the particle reference frame (see later in this section), a, b are the semi-major and semi-minor length of the rod, respectively, and η is a sharpness parameter that controls the sharpness of the super-ellipsoid edge. We use $\eta = 1$for ellipsoids and $\eta = 4$ for cylinders (i.e. we consider cylinders with rounded edges, see Fig. 1a). For spherocylinders, we use

$$f\left(x', y', z'\right) = 1 \tag{3}$$

where

$$f\left(x', y', z'\right) = \begin{cases} \frac{y'^2}{b^2} + \frac{z'^2}{b^2}, & \left|x'\right| < a - b \\ \left(\frac{x'}{b} - \frac{x'}{|x'|}\left(\frac{a}{b} - 1\right)\right)^2 + \frac{y'^2}{b^2} + \frac{z'^2}{b^2}, & \left|x'\right| \geq a - b \end{cases} \tag{4}$$

For all the particle shapes above, we consider rods with aspect ratio $a/b = 2.5$.

For the cylindrical sessile drop, we consider a drop with a rectangular base with width $W = 20b$ (i.e. 4 times the length of the rods) and length $L = 2a + 25b$ (i.e. 6 times the length of the rods). For convenience, we refer to the top and bottom fluid phases as oil and water, respectively (i.e. the fluid making up the drop is water), though our model is in fact general and applies to any fluid–fluid interface. Assuming the origin of the laboratory frame in Cartesian coordinates to be at the centre of the base with z perpendicular to the base and x, y parallel and perpendicular to the long axis of the cylinder, respectively, we assume that the contact

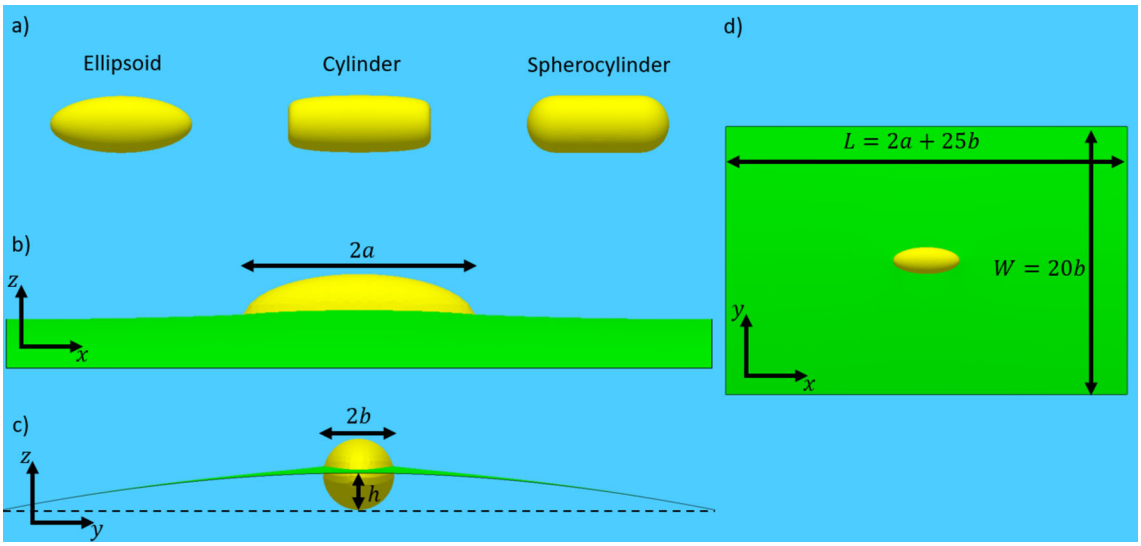

Fig. 1 **a** Geometry of the rod-like particles studied in our simulations. All particles have aspect ratio $a/b = 2.5$. **b–d** Geometry of an ellipsoidal particle adsorbed to the simulation interface with views from the **b** side, **c** end and **d** top

lines of the cylindrical drop are pinned at $y = \pm W/2$ and apply reflecting boundary conditions at the ends of the cylindrical drop at $x = \pm L/2$ (Fig. 1b, d). We chose L to be as large as possible to minimise finite size effects due to the reflecting boundaries at the cylindrical drop ends while still being computationally feasible. To validate that finite size effects are negligible for our choice of L, for selected cases, we increased L by 50% and found that this led to a change in our calculated results of less than 3% (see Figure S1 in Supplementary Information).

We control the curvature of the sessile drop by applying a Laplace pressure of γ_{ow}/R across the interface in our simulations, where R is the radius of curvature of the cylindrical interface in absence of any adsorbed particles, and γ_{ow} is the oil–water interfacial tension. Although the behaviour of adsorbed rods is controlled by the curvature of the cylindrical drop, it is easier to control and measure the height of the drop experimentally. For convenience, we therefore parameterise the curvature of the drop using the drop height in the absence of adsorbed particles, h (Fig. 1c), which is related to R and W according to $R = h/2 + W^2/8h$.

In this paper, we focus on the immersion regime and it is therefore important to calculate h_t, the value of h where an adsorbed rod in its equilibrium configuration just touches the solid substrate, since h_t demarcates the boundary between the immersion and flotation regimes. Specifically, if we denote Δr as the equilibrium height of the rod centre above h in the absence of a solid substrate, then from Fig. 1c, h_t is the value of h that satisfies the condition $h + \Delta r = b$ (noting that Δr is a function of h). In Fig. S4 of Supplementary Information, we use this method to calculate h_t for the different particle shapes and contact angles studied in this paper and the results are listed in Table 1. Note that as expected, the value of h_t for any given particle shape decreases as we go from hydrophilic to neutral to hydrophobic particles. The immersion regime is defined as the case where $h < h_t$. For rod-like particles in the immersion regime, the rods sit on the solid substrate with their long axis parallel to the solid substrate and their centre heights fixed to be $z_p = b$. To specify the position of the rods on the substrate, we use the position of the rod centre parallel and perpendicular to the long axis of the cylindrical drop which we denote as x_p and y_p, respectively (Fig. 2a, x_p not shown). To specify the orientation of the adsorbed rods, we use the angle of their long axis to the long axis of the cylindrical drop which we denote as the bond angle θ_b (Fig. 2b). Note that we only need one angle to specify orientation since all the rod shapes we consider in this paper are axisymmetric. Later on we also perform some simulations of particles in the flotation regime ($h > h_t$), and when doing so, we also allow the height of the particle relative to the interface to be equilibrated for a given particle configuration. We define the particle reference frame x', y', z' such that its origin coincides with the centre of the rod, x' lies along the semi-major axis of the rod, while y' and z' lie along the semi-minor axes of the rod with z' parallel to substrate normal. The particle frame coordinates x', y', z' are readily related to the laboratory frame coordinates (x, y, z) using appropriate rotation transformations. [32]

Table 1 Values for h_t, the flotation to immersion transition height, for the particle shapes and contact angles studied in this paper

Contact angle/shape	Ellipsoid	Cylinder	Spherocylinder
70°	1.1b	1.2b	1.2b
90°	1.0b	1.0b	1.0b
110°	0.75b	0.7b	0.7b

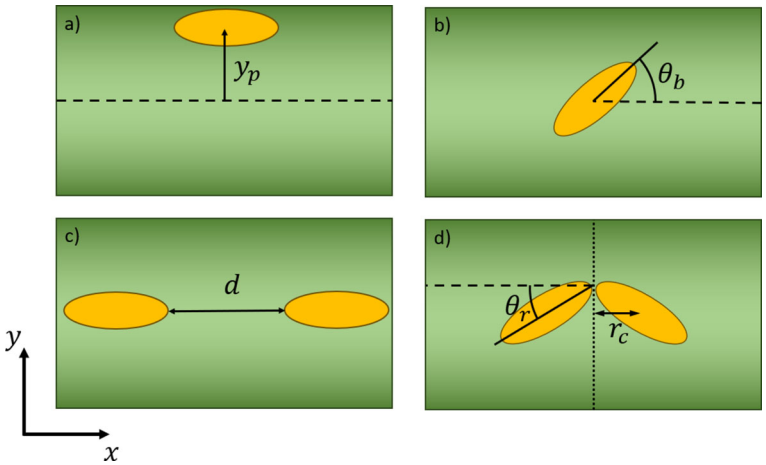

Fig. 2 Coordinates characterising single- and two-particle configurations: **a** lateral displacement, **b** bond angle, **c** tip-to-tip separation, **d** roll-over angle

When studying the capillary interaction and self-assembly of two rods later, we will primarily focus on rods in the tip-to-tip configuration (with $y_p = 0$) and we specify the separation of the two rods in this case by their surface-to-surface separation d (Fig. 2c). As we shall see later in the paper, in some regions of system parameter space, the immersion capillary forces are so strong that they drive two rods in the tip-to-tip configuration to first come into tip-to-tip contact, then 'roll-over' into side-to-side contact [18, 22]. To study this roll-over transition, we define the roll-over angle θ_r, which is the angle that two mirror-symmetric rods make to the long axis of the cylindrical drop as shown in Fig. 2d. Note that the two particles are in contact with $y_p = 0$ throughout the transition.

The energy of the adsorbed rod system is primarily due to the interfacial energy and is given by [34, 35].

$$E_{\text{int}} = \gamma_{\text{ow}} A_{\text{ow}} + \gamma_{\text{po}} A_{\text{po}} + \gamma_{\text{pw}} A_{\text{pw}} \tag{5}$$

where γ_{ow}, γ_{po} and γ_{pw} are the interfacial tensions and A_{ow}, A_{po} and A_{pw} are the areas of the oil–water, particle–oil and particle–water interfaces, respectively. We have neglected line tension contributions in Eq. (5) because these are sub-dominant compared to interfacial tensions for the particle sizes we are considering where $a, b \geq 10\,\text{nm}$ [36]. We can simplify Eq. (5) by eliminating one of the interfaces from the problem. For example, using $A_{\text{pw}} = A - A_{\text{po}}$ (where A is the total area of the particle), Young's equation $\gamma_{\text{ow}}\cos\theta_w = \gamma_{\text{po}} - \gamma_{\text{pw}}$ (where θ_w is the contact angle) and dropping irrelevant constant terms, we find

$$E_{\text{int}} = \gamma\left(A_{\text{ow}} + \cos\theta_w A_{\text{po}}\right) \tag{6}$$

i.e. we have eliminated the particle–water interface and can model the system by just simulating the oil–water interface (with interfacial tension γ) and the particle-oil interface (with effective interfacial tension $\gamma\cos\theta_w$) and we use γ to denote the oil–water interfacial tension in what follows for simplicity.

For a given particle configuration, the interfacial energy of the system given by Eq. (6) (or its equivalent obtained from eliminating the particle-oil interface) is calculated using Surface Evolver [33]. This is a finite element software that minimises the energy of the system subject to constraints like boundary conditions of the simulation box, particle geometry and the Laplace pressure [33–35, 37]. The minimisation is performed by representing the surface as a mesh of triangles and adjusting the position of vertices using a steepest descent method. The constant contact angle requirement around the particle is automatically satisfied within this scheme since Young's equation arises from the minimisation of the total interfacial energy. Note that

since we are using an energy minimising scheme, we are calculating the equilibrium state of the system. Non-equilibrium phenomena such as contact line pinning [38, 39], friction with the substrate (relevant in the immersion regime) and evaporative fluxes when we dry the droplet will affect the dynamics of how the system approaches equilibrium, and in some cases may even cause the system to be trapped in metastable states and prevent the system from reaching equilibrium. These forces may be important in specific experimental realisations of our system, but the inclusion of these effects lies beyond the scope of our study.

In the simulations, we work with length and energy units such that $b = 1$, $\gamma = 1$ and use a variable triangular mesh edge length between $0.04b$ and $0.2b$ and quadratic edges to capture the shape of the liquid interface and three-phase contact line more accurately. To validate that our results are not significantly affected by our choice of mesh size, for selected cases, we reduced the mesh edge length to between $0.03b$ and $0.15b$ (i.e. doubling the number of mesh points) and found that this led to a change in the calculated interfacial energy of less than 1% (see Fig. S2 in Supplementary Information). Finally, when assessing whether a confining potential is strong or weak in this paper, we compare the potential to the thermal energy $k_B T$, the energy scale of background thermal fluctuations which become important on the nanoscale. This comparison allows us to determine whether the confinement or assembly of the particles due to the potential is stable against the randomising effect of thermal fluctuations under quiescent conditions.

3 Results and discussion

3.1 Orientational transition of single rods

In this section, we consider the impact of particle shape, contact angle and cylindrical drop height on the orientation of single adsorbed rods in the immersion regime, as specified by the bond angle θ_b (Fig. 2a). As we shall see later in Sect. 3.2, adsorbed rods are strongly confined to lie along the centreline of the cylindrical drop in the immersion regime and we therefore set $y_p = 0$ in our simulations. In addition, since we are interested in studying the behaviour of isolated adsorbed rods in this section, we set $x_p = 0$, i.e. the particles are situated at the centre of simulation box to minimise the impact of the reflecting boundary conditions at the cylindrical drop ends. We then calculate the energy of the system as a function of bond angle from $\theta_b = 0°$ to $90°$ in increments of $1°$, noting that the energy only needs to be calculated for this range due to the symmetry of the energy with respect to θ_b.

In Fig. 3 we plot the orientational energy curves, i.e. interfacial energy (relative to the minimum energy state) as a function of bond angle θ_b, for ellipsoids, cylinders and spherocylinders (first, second and third row, respectively), drop heights $h = h_t$, $0.75h_t$, $0.5h_t$ (first, second and third column, respectively) and contact angles $\theta_w = 70°$, $90°$, $110°$ (i.e. hydrophilic, neutral and hydrophobic rods, respectively), with the value of h_t for the different cases given in Table 1.

We first consider the orientation of the rods at the transition height $h = h_t$, i.e. first column of Fig. 3. We see that in this case, the equilibrium orientation of the different rod shapes (i.e. θ_b corresponding to the energy minimum) can be engineered to lie either parallel ($\theta_b = 0°$) or perpendicular ($\theta_b = 90°$) to the long axis of the cylindrical drop by tuning the contact angle. In particular, we see that hydrophilic ellipsoids lie perpendicular, while neutral and hydrophobic ellipsoids lie parallel to the cylindrical drop (Fig. 3a); on the other hand, hydrophilic cylinders lie parallel, while neutral and hydrophobic cylinders lie perpendicular to the cylindrical drop (Fig. 3b). These results are similar to those reported for ellipsoids and cylinders in the flotation regime ($h > h_t$) [32]. This fact is not surprising since for $h = h_t$, we expect the monopolar deformation of the liquid meniscus due to the protrusion of the rod above the cylindrical drop to be relatively weak so that the orientational behaviour of the rods is determined by the quadrupolar deformation of the liquid meniscus, similar to the flotation case (see later in Fig. 4). Specifically, the capillary quadrupole will align its rise axis with the principle axis of curvature of the cylindrical interface (where the interface is concave up) in order to minimise the distortion to the host interface [27–29]. This is why hydrophilic ellipsoids align perpendicular since they have a rise axis at their sides, while hydrophobic ellipsoids align parallel since they have their rise axis at their tips. The trend is reversed for cylinders since the curvature of their capillary quadrupole is opposite to that of ellipsoids for a given contact angle. [32]

Interestingly, the dependence of particle orientation on contact angle for spherocylinders is different at $h = h_t$ (Fig. 3c) compared to the behaviour in the flotation regime. Specifically, spherocylinders are always aligned parallel regardless of contact angle in the flotation regime [32], while at $h = h_t$, hydrophilic and neutral spherocylinders are aligned parallel, while hydrophobic spherocylinders are aligned perpendicular.

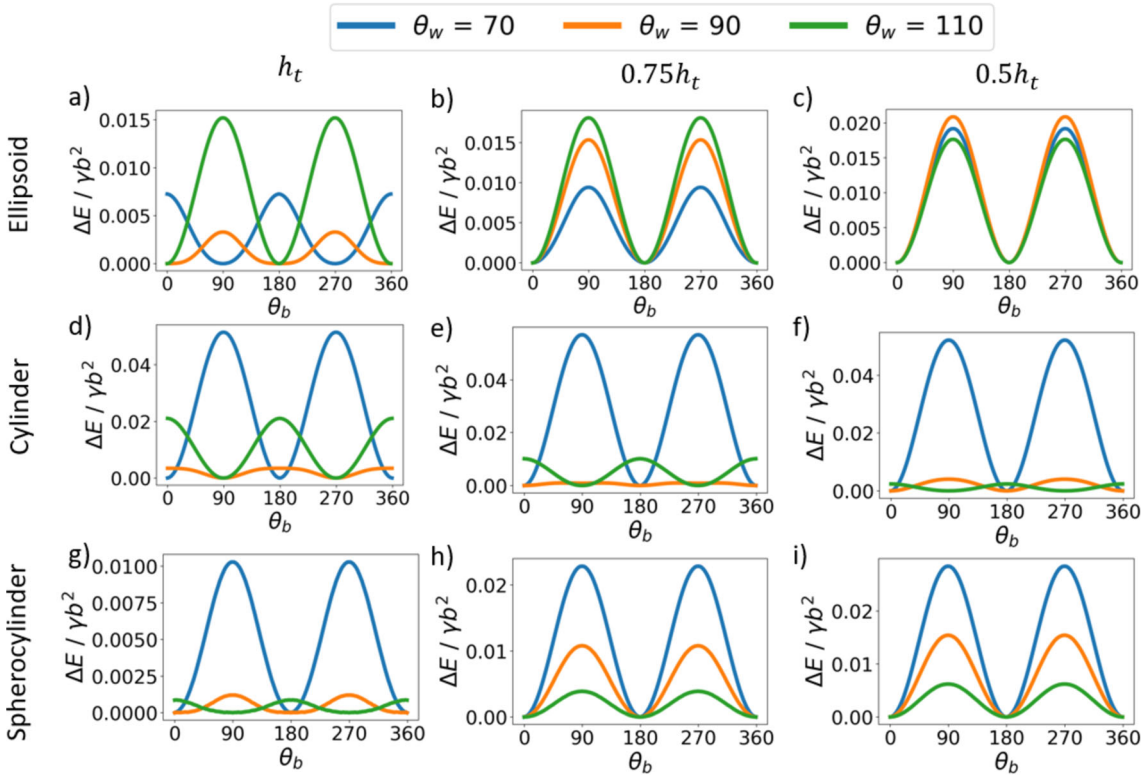

Fig. 3 Interfacial energy (relative to the minimum energy state) as a function of bond angle θ_b for different particle shapes, drop heights and contact angle θ_w

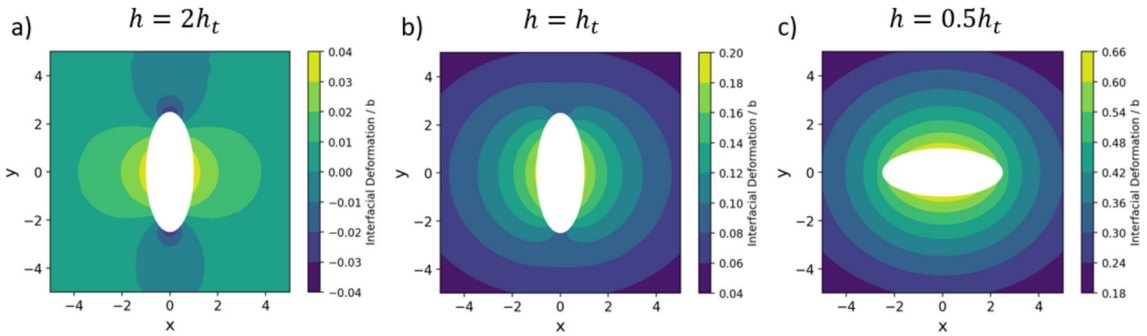

Fig. 4 **a** Meniscus deformation around an ellipsoidal particle with contact angle $\theta_w = 70°$ adsorbed at a cylindrical drop for drop heights of **a** $2h_t$ (flotation regime), **b** h_t (transition height), **c** $0.5h_t$ (immersion regime). The long axis of the cylindrical drop is in the x direction, and the ellipsoid is in its equilibrium orientation at each height

This difference is not surprising since spherocylinders do not possess an intrinsic capillary quadrupole, so the dependence of particle orientation on contact angle is more subtle and harder to predict a priori. The absence of an intrinsic capillary quadrupole in spherocylinders is also evidenced by the fact that the energy scales in the orientational energy curves for spherocylinders (Fig. 3g) are significantly smaller than that for ellipsoids and cylinders (Fig. 3a, d).

In addition to the curvature of the capillary quadrupole, another important factor determining the orientation of rods at a cylindrical interface is particle anisotropy. For $h \geq h_t$, the effect of particle anisotropy arises from the fact that, because of the curvature of the cylindrical interface, a rod-like particle removes a larger area of the energetically unfavourable oil–water interface when it is parallel rather than perpendicular to the cylindrical drop. Particle anisotropy therefore favours the parallel orientation compared to the perpendicular orientation. This effect explains why for non-neutrally wetting rods in Fig. 3a, d, g, the potential energy well depth for the parallel orientation is significantly greater than for the perpendicular orientation. Specifically, for non-

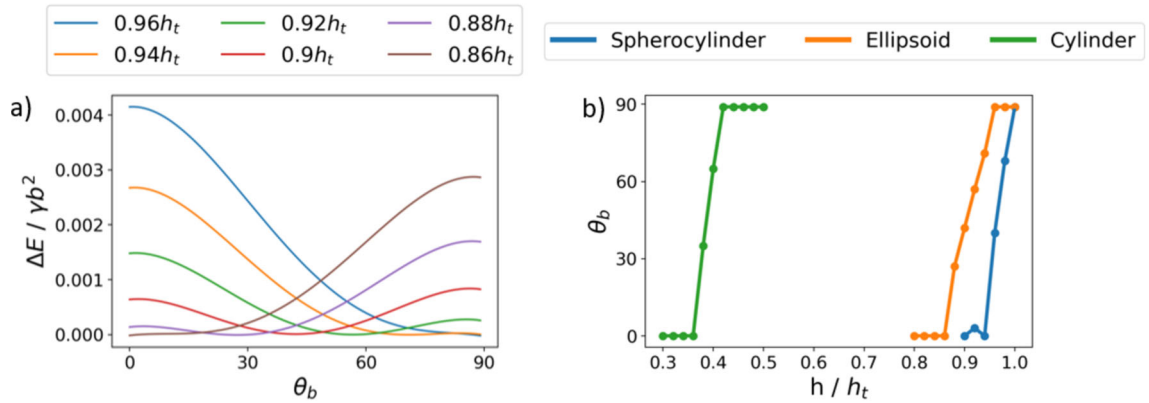

Fig. 5 **a** Interfacial energy (relative to minimum energy state) as a function of bond angle for adsorbed ellipsoids with contact angle $\theta_w = 70°$ for different cylindrical drop heights around the orientational transition. **b** Equilibrium bond angle as a function of cylindrical drop height for ellipsoids with $\theta_w = 70°$, cylinders with $\theta_w = 110°$ and spherocylinders with $\theta_w = 110°$

neutrally wetting rods in the parallel orientation, both contact line curvature and particle anisotropy favour parallel alignment, i.e. the two effects are synergetic. On the other hand, for non-neutrally wetting rods in the perpendicular orientation, contact line curvature favours perpendicular alignment, but particle anisotropy favours parallel alignment, i.e. the two effects are antagonistic.

We next consider the effect of decreasing cylindrical drop height below h_t on the orientation of the rods, starting with the case of ellipsoids and spherocylinders (first and third row in Fig. 3). We see that as we decrease drop height to $h = 0.75h_t$ and $0.5h_t$, ellipsoids and spherocylinders align parallel to the cylindrical drop regardless of contact angle. The parallel alignment of these rods comes from the fact that as we decrease h, there is now significant monopolar deformation of the liquid meniscus so that the orientation of the rods is now controlled by monopolar deformations rather than by the capillary quadrupole of the rods. Specifically, the shape anisotropy of the rods means that they create larger monopolar deformations when they are in the perpendicular orientation compared to the parallel orientation since their ends protrude above the cylindrical interface more in the perpendicular orientation, making the parallel orientation more energetically favourable. Not surprisingly, this effect becomes stronger as we decrease h, as can be seen from the fact that the potential energy well depth for the parallel orientation increases for both ellipsoids and spherocylinders as we go from $h = 0.75h_t$ to $h = 0.5h_t$.

While particle anisotropy plays the dominant role in determining particle orientation in the immersion regime, the effect of contact line curvature is still significant. This can be seen from the fact that for $h = 0.75h_t$, $0.5h_t$, the potential energy well depth for parallel orientation is largest for hydrophobic ellipsoids and hydrophilic spherocylinders, i.e. where contact line curvature and particle anisotropy both favour the parallel orientation so that the two effects are synergetic. On the other hand, the potential energy well depth is smallest for hydrophilic ellipsoids and hydrophobic spherocylinders, i.e. where contact line curvature favours the perpendicular orientation, but particle anisotropy favours the parallel orientation so that the two effects are antagonistic.

We next consider the case of cylinders (second row in Fig. 3). As we decrease the drop height to $h = 0.75h_t$ and $0.5h_t$, we see that particle anisotropy again drives the rods towards the parallel orientation, so that both hydrophilic and neutral cylinders now have parallel orientation, while the potential energy well depth for perpendicular orientation for hydrophobic cylinders is significantly reduced. However, hydrophobic cylinders are still in the perpendicular orientation even at $h = 0.5h_t$, and we have to decrease h below $0.4h_t$ before this system transitions to the parallel orientation (see later in Fig. 5b). We believe that the much lower values of h required to drive hydrophobic cylinders into the parallel orientation arise from the fact that for cylinders that are in the perpendicular orientation, their flat ends allow them to accommodate different interfacial heights more readily compared to particles with rounded ends such as ellipsoids and spherocylinders. This means that we need to go to much lower values of h before the system can generate large enough monopolar deformations to drive cylinders into the parallel orientation.

In the preceding discussion, we have assumed that the orientation of the adsorbed rods is primarily determined by quadrupole deformations of the liquid meniscus for $h = h_t$ and by monopolar deformations of the liquid meniscus for $h < h_t$. To confirm that this is indeed the case, we analyse in more detail how the multi-

polar character of the liquid meniscus changes as we change the drop height across h_t. In Fig. 4a, b, c, we plot the deformation of the liquid interface (relative to the unperturbed cylindrical interface) around an adsorbed hydrophilic ellipsoid (contact angle $\theta_w = 90°$) for $h = 2h_t$, h_t, $0.5h_t$, respectively; note that this ellipsoid has a perpendicular orientation for $h = 2h_t$, h_t and a parallel orientation for $h = 0.5h_t$ (see Fig. 3). From Fig. 4, we see that the interfacial deformation is quadrupolar for $h = 2h_t$ (Fig. 4a), monopolar for $h = 0.5h_t$ (Fig. 4c) and a combination between the two for $h = h_t$, specifically quadrupolar in the near-field but monopolar in the far-field (Fig. 4b). These results confirm that quadrupolar deformations are only significant for $h \geq h_t$, while monopolar deformations become dominant for $h < h_t$. To help visualise the meniscus deformations in Fig. 4 more clearly, in Fig. S7 in Supplementary Information, we also show 3D plots of the meniscus deformation for $h = 2h_t$ and $h = 0.5h_t$.

In Fig. 3, we saw that as we decrease h, rods that were initially in the perpendicular orientation at $h = h_t$ undergo a transition to the parallel orientation due to monopolar interfacial deformations becoming increasingly dominant over quadrupolar deformations. We now study this transition in more detail. In Fig. 5a, we plot the orientational energy curves from $\theta_b = 0°$ to $90°$ for ellipsoids with contact angle $\theta_w = 70°$ at the different drop heights over which the orientational transition occurs (around $0.9h_t$). Note that the energy scales of orientational energy curves become quite small close to an orientational transition and the energy curves can therefore be quite noisy due to the reduced signal-to-noise ratio. To obtain smooth energy curves so that we can identify minima and maxima accurately, we therefore filter the simulated energy curves before analysing them. Details of the filtering procedure can be found in Supplementary Information (see Fig. S5, S6,) and the curves shown in Fig. 5 are based on the filtered energy curves.

From Fig. 5a, we see that each orientational energy curve only has one minimum and the position of this minimum decreases continuously from $\theta_b = 90°$ (perpendicular orientation) to $\theta_b = 0°$ (parallel orientation) as h is decreased. We therefore conclude that the orientational transition for hydrophilic ellipsoids is a second-order (or continuous) transition. In Fig. S6 in Supplementary Information, we show the corresponding orientational energy curves for hydrophobic cylinders and hydrophobic spherocylinders and we see that the orientational transition for these rods is also continuous transitions. The results for all three orientational transitions are summarised in Fig. 5b where we plot the equilibrium bond angle as a function of cylindrical drop height for each of the three rods. As expected, as we decrease h, the equilibrium bond angle decreases continuously from the perpendicular orientation to the parallel orientation for all three rods. Interestingly, the transition for cylinders occurs at significantly lower drop heights compared to ellipsoids or spherocylinders. As discussed earlier, we believe that this difference is due to the fact that when the rods are in the perpendicular orientation, the flat ends of the cylinder allow it to accommodate different interfacial heights more readily compared to particles with rounded ends such as ellipsoids and spherocylinders. This means that we need to go to much lower values of h before the energy penalty from the monopolar deformations is large enough to drive cylinders into the parallel orientation.

The results in Figs. 3, 4 and 5 show that for low enough cylindrical drop heights, all adsorbed rods will orientate themselves parallel to the long axis of the cylindrical drop, regardless of the shape or contact angle of the rods. Working with adsorbed rods in the immersion regime thus provides a robust method for preparing rods in the parallel orientation.

3.2 Orientational and spatial confinement of single rods

In the previous section, we studied how we can control the orientation of adsorbed rods in the immersion regime by changing particle shape, contact angle and cylindrical drop height. In this section, we study how the strength of the orientational confinement and spatial confinement of the adsorbed rods changes as we go from the flotation regime ($h > h_t$) to the immersion regime ($h < h_t$). To simplify our discussion, we focus on the case where the adsorbed rods are aligned parallel to the cylindrical drop as this is the most favourable alignment for achieving the tip-to-tip assembly considered in the next section. Specifically, we consider the behaviour of ellipsoids with $\theta_w = 110°$, cylinders with $\theta_w = 70°$, and spherocylinders with $\theta_w = 70°$ in this section.

In Fig. 6a–c we plot the orientational energy curves from $\theta_b = 0°$ to $90°$ for hydrophobic ellipsoids, hydrophilic cylinders and hydrophilic spherocylinders, respectively, for drop heights of $h = 2h_t$, h_t and $0.5h_t$. Note that for the results in Fig. 6, we set x_p, $y_p = 0$ as in the previous section, and the equilibrium orientation is the parallel orientation $\theta_b = 0°$ in all cases. For ellipsoids and cylinders (Fig. 6a, b), we see that the well depth for the orientational energy curves is greater for $h = 2h_t$ compared to $h = 0.5h_t$, i.e. the orientational

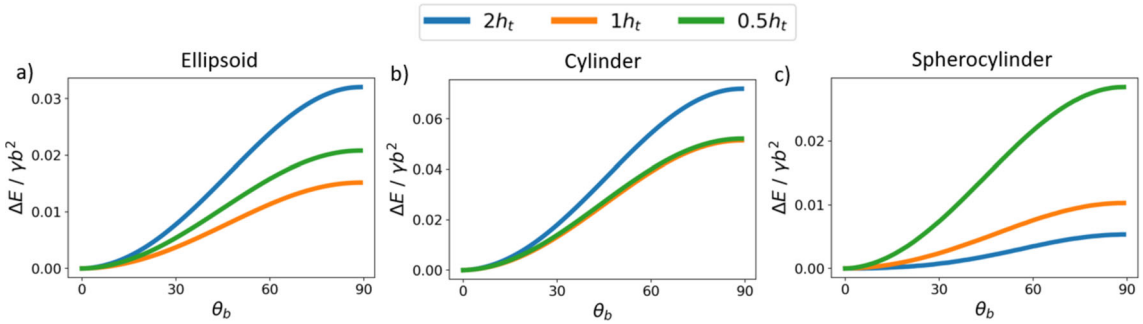

Fig. 6 Interfacial energy (relative to energy at $\theta_b = 0°$) as a function of bond angle θ_b for different cylindrical drop heights for: **a** ellipsoids with $\theta_w = 110°$, **b** cylinders with $\theta_w = 70°$, **c** spherocylinders with $\theta_w = 70°$

confinement of the rods is stronger in the flotation regime compared to in the immersion regime. This is not surprising since the confining potential due to interfacial curvature is proportional to the product of the deviatoric curvature of the host interface and the capillary quadrupole of the adsorbed particle [28, 29, 32] and the deviatoric curvature of the cylindrical drop decreases as we reduce h.

From Fig. 6a, b, we note that there is a slight increase in the orientational confinement of ellipsoids and cylinders when we reduce the drop height from $h = h_t$ to $h = 0.5h_t$. As discussed in the previous section, this increase comes from the fact that in the immersion regime, particle orientation is determined not only by interfacial curvature, but also by monopolar deformations of the interface. Specifically, since larger monopolar deformations are generated in the perpendicular orientation compared to in the parallel orientation, monopolar forces drive the rods into the parallel orientation, and this effect becomes stronger as we reduce h. Once again, the increase in the confining potential is smaller for cylinders compared to ellipsoids because the flat ends of the cylinder allow it to accommodate different interfacial heights more readily when it is in the perpendicular orientation compared to ellipsoids, thus reducing the monopolar driving force for the parallel orientation.

Interestingly, from Fig. 6c, we see that for hydrophilic spherocylinders, the orientational confinement is stronger for $h = 0.5h_t$ (immersion regime) compared to for $h = 2h_t$ (flotation regime). This result can be understood from the fact that spherocylinders do not have an intrinsic capillary quadrupole so that the orientational confinement due to interfacial curvature is weak, as evidenced by the fact that the confining potential at $h = 2h_t$ is significantly smaller for spherocylinders compared to ellipsoids and cylinders. This means that the dominant contribution to orientational confinement for spherocylinders comes from monopolar immersion forces, which increase as we decrease h.

It is important to emphasise that although the orientational confinement of the rods is weaker in the immersion regime for some rod shapes, the confinement is still significant for all the rods studied above. Specifically, the well depth of the confining potential at $h = 0.5h_t$ is $\approx 0.02\gamma b^2$ for the ellipsoid, $\approx 0.05\gamma b^2$ for the cylinder and $\approx 0.03\gamma b^2$ for the spherocylinder. For nanoscale rods with $b = 10$ nm adsorbed at an oil–water interface with $\gamma = 30 \times 10^{-3}$ N/m, this translates to well depths of $\approx 15k_BT$, $\approx 40k_BT$ and $\approx 20k_BT$, respectively. This means that the orientational confinement is significant in the immersion regime even for nanorods.

In order to study the spatial confinement of the rods lateral to the cylindrical drop, in Fig. 7a–c we plot interfacial energy (relative to the value at $y_p = 0$) as a function of lateral displacement y_p for hydrophobic ellipsoids, hydrophilic cylinders and hydrophilic spherocylinders, respectively, for drop heights of $h = 2h_t$, h_t and $0.5h_t$. For the results in Fig. 7, we set $\theta_b = 0°$ since all rods have a parallel equilibrium orientation, and we set $x_p = 0$ to minimise the impact of the reflecting boundary conditions at the cylindrical drop ends in our simulations. We see that for all the rods, the spatial confinement of the adsorbed rods to the centreline of the cylindrical drop ($y_p = 0$) in the flotation regime (i.e. for $h = 2h_t$, h_t) is very weak compared to in the immersion regime (i.e. for $h = 0.5h_t$). As discussed in ref.32, the very weak spatial confinement in the flotation regime is due to the fact that cylindrical drops have no curvature gradients which we can use to control particle position, and the spatial confinement comes only from the capillary repulsion between the capillary quadrupole of the rods and the pinned contact lines of the sessile drop which is weak and short ranged [40, 41]. In contrast, the spatial confinement is very strong in the immersion regime because the confinement is due to monopolar deformations of the liquid interface that come from the mismatch in the height of the rod three-phase contact line compared to the local height of the cylindrical drop, and this mismatch becomes greater for larger lateral displacements of the rod.

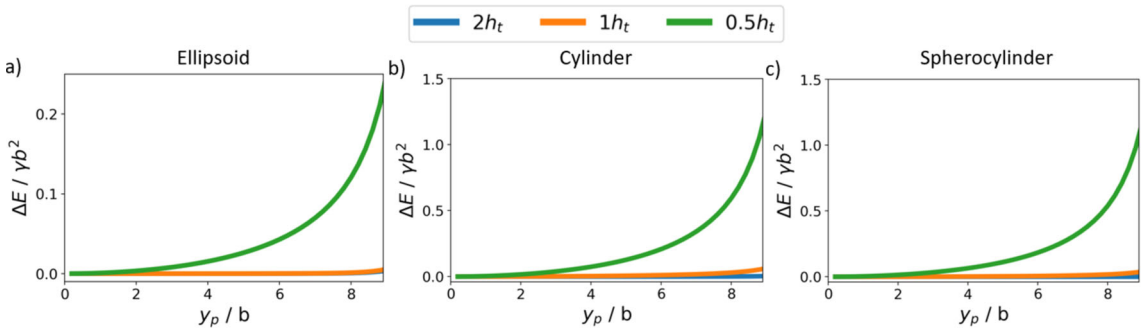

Fig. 7 Interfacial energy (relative to value at $y_p = 0$) as a function of lateral displacement y_p for different cylindrical drop heights for **a** ellipsoids with $\theta_w = 110°$, **b** cylinders with $\theta_w = 70°$, **c** spherocylinders with $\theta_w = 70°$. Note that the $h = 2h_t$ line in (**a**) cannot be seen as it lies underneath the $h = h_t$ line

Interestingly, from Fig. 7 we see that confining potential for both cylinders and spherocylinders (Fig. 7b, c) is significantly greater compared to ellipsoids (Fig. 7a). We believe that this difference is due to the tips of the ellipsoid being much more rounded compared to cylinders and spherocylinders. This means that for ellipsoids, the monopolar deformations of interface only occur along the middle portion of the rod as the bottom surface of the tips lies above the cylindrical interface, while for cylinders and spherocylinders, the monopolar deformations essentially occur along the whole length of the rod. Notwithstanding this difference, the spatial confinement for all the different rod shapes in Fig. 7 is very strong in the immersion regime. Specifically, for $h = 0.5h_t$ the well depth of the spatial confining potential (i.e. the potential at $y_p = 9b$, the largest value of y_p that we could access numerically, compared to at $y_p = 0$) is $0.25\gamma b^2$, $1.3\gamma b^2$ and $1.2\gamma b^2$, respectively, for the ellipsoids, cylinders and spherocylinders, which translates to $180k_BT$, $920k_BT$ and $860k_BT$ for $b = 10$ nm and $\gamma \approx 30 \times 10^{-3}$ N/m. In summary, by working in the immersion regime, we can achieve strong orientational and spatial confinement of the adsorbed rods, even in the case of nanorods.

3.3 Capillary interaction and self-assembly for two rods

Having considered both the orientational and lateral confinement of single particles at a cylindrical interface in the previous section, in this section we consider the interaction and self-assembly of two rods at the cylindrical interface in the immersion regime. To simplify our discussion, we focus on the tip-to-tip interaction and assembly of adsorbed rods and therefore we restrict our analysis to rods with parallel alignment, specifically ellipsoids with $\theta_w = 110°$, cylinders with $\theta_w = 70°$ and spherocylinders with $\theta_w = 70°$. Since our focus is on two-particle configurations that are mirror symmetric (see Fig. 2c, d), we can simplify our calculations by exploiting the fact that the energy of the two-particle system where both rods are approaching each other is equal to twice the energy of one rod approaching the reflecting boundary of cylindrical drop end. We therefore calculate the energy of the two-rod system by considering a one-rod simulation where we vary the distance of the rod from the reflecting boundary. Since, as we saw in the previous section, the adsorbed rods are strongly confined to the centreline of the cylindrical drop in the immersion regime, we set $y_p = 0$ in our simulations.

We first consider the capillary interactions between two rods in the tip-to-tip configuration (see Fig. 2c), i.e. we set $\theta_b = 0°$ in our simulations. In Fig. 8a–c, we plot the tip-to-tip capillary interaction energy (i.e. energy relative to the energy of the two rods at maximum separation) as a function of the surface-to-surface separation between the rods d for the ellipsoid, cylinder and spherocylinder, respectively, for $h = 2h_t$, h_t and $0.5h_t$. We see that in all cases, the strength and range of the capillary interaction increase dramatically as we go from $h = 2h_t$ (flotation regime) to $h = 0.5h_t$ (immersion regime). This is not surprising since particle interactions in the flotation regime are quadrupolar and therefore weak and short ranged (negligible beyond one rod length away) [32], while those in the immersion regime are monopolar and therefore strong and long ranged (significant up to 4–5 rod lengths away) [11, 15].

Interestingly, we see from Fig. 8 that the strength of the capillary interactions in the immersion regime decreases as we go from cylinders to spherocylinders to ellipsoids. We believe that this trend is due to the increasingly rounded nature of the particle tips for this sequence of particle shapes which means that the monopolar deformations near the tips occur over a smaller and smaller effective cross-sectional area. Notwithstanding this fact, the capillary bond energy at contact is very large for all the particles in the immersion regime.

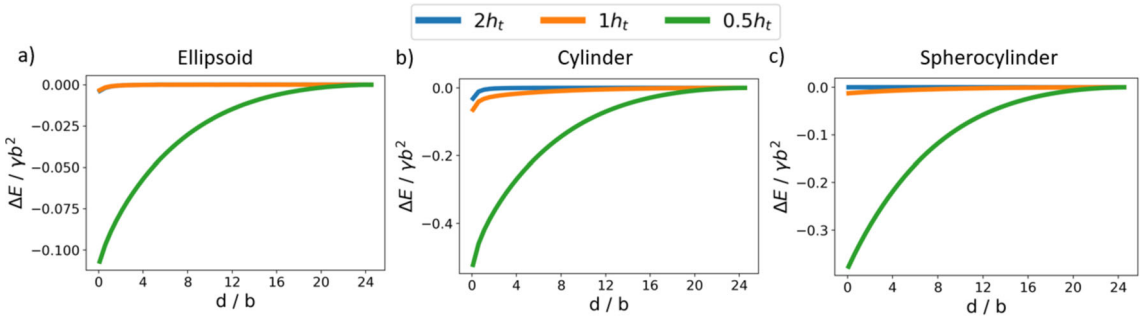

Fig. 8 Capillary interaction energy between two particles in the tip-to-tip configuration as a function of surface-to-surface separation d for different drop heights for: **a** ellipsoids with $\theta_w = 110°$, **b** cylinders with $\theta_w = 70°$, **c** spherocylinders with $\theta_w = 70°$. Note that the curve for $h = 2h_t$ in (**a**) cannot be seen as it lies beneath the curve for $h = h_t$

Specifically, for $h = 0.5h_t$, the capillary bond energy is $0.11\gamma b^2$, $0.52\gamma b^2$ and $0.38\gamma b^2$, respectively, for the ellipsoids, cylinders and spherocylinders, which translates to $78k_BT$, $380k_BT$ and $270k_BT$ for $b = 10$ nm and $\gamma \approx 30 \times 10^{-3}$ N/m.

For parallel rods in the immersion regime, the strong spatial confinement transverse to the cylindrical drop and tip-to-tip capillary interactions between the rods provide a strong driving force for them to form tip-to-tip clusters. However, from the preceding discussion, we see that as we decrease the cylindrical drop height h in the immersion regime, the capillary interaction increases dramatically (Fig. 8), but the orientational confinement does change significantly (Fig. 6). We therefore anticipate that if we decrease h too much, we may destabilise the tip-to-tip clusters that are formed since the system can lower its energy by undergoing a roll-over transition to the side-to-side configuration which has a smaller centre-to-centre separation between the rods at contact; note that this transition is also seen for ellipsoids at a flat interface [18, 22]. In what follows, we consider the mechanical stability of tip-to-tip clusters in our system against the roll-over transition as we change h in the immersion regime.

We note that the roll-over transition occurs when the two rods in the cluster pivot about their contacting tips in a mirror-symmetric configuration as shown in Fig. 2d, where the configuration of the cluster during the transition is characterised by the roll-over angle θ_r. Our first task is therefore to calculate the perpendicular distance of each rod centre from the mirror plane r_c as a function of θ_r. For spherocylinders, r_c can be calculated from simple geometry to be $r_c = (a - b)\cos\theta_r + b$. For superellipsoids given by Eqs. (1) and (2), r_c can be calculated as follows. We first set $z' = 0$ in Eqs. (1) and (2) since the contact point lies in the $z' = 0$ plane. We next note that the surface normal vector for the rod is given by ∇f, where $f(x', y', z')$ is given by Eq. (2) and ∇ is the 3D grad vector in the laboratory frame. Since the surface normal vector points in the x direction at the contact point by symmetry, the contact point coordinate satisfies $\partial f/\partial y = 0$. This equation, together with Eqs. (1) and (2), gives us two simultaneous equations which we can solve to find the contact point coordinate (x_c, y_c) and r_c is then given by $r_c = x_c - x_p$. In the case of ellipsoids ($\eta = 1$), we can obtain an analytical expression for r_c as a function of θ_r using this procedure [37]. In the case of cylinders ($\eta = 4$), we can calculate r_c as a function of θ_r numerically using this procedure. Having found r_c for the different rod shapes, we fix x_p such that the rod centre is a distance $r_c + \Delta$ away from the reflecting boundary, where we include a thin exclusion zone of thickness $\Delta = 0.05b$ around each rod to avoid the numerical issues that occur when the rod is in contact with the reflecting boundary. To validate that our results are not significantly affected by our choice of Δ, for selected cases we used $\Delta = 0.075b$ and found that this led to a shift in the roll-over transition heights of less than 4% (see Fig. S3 in Supplementary Information).

In Fig. 9a, we plot the interfacial energy (relative to the value at $\theta_r = 0°$) as a function of θ_r for hydrophilic ellipsoids for different drop heights h around the roll-over transition. Note that the energy curves in Fig. 9 have been filtered in the same way as in Fig. 5 to reduce noise and allow us to identify the minima and maxima points more accurately (see Supplementary Information). From Fig. 9a, we see that at large h (e.g. the blue curve), there is a single minimum at $\theta_r = 0°$ corresponding to the tip-to-tip configuration, but as we decrease h below a critical value, the energy curve develops a local minimum at $\theta_r = 90°$ corresponding to the side-to-side configuration, which is separated from the primary minimum at $\theta_r = 0°$ by an energy barrier. As h is decreased further to $h_b = 0.36b$ (green curve), the energy of the side-to-side configuration becomes equal to that of the tip-to-tip configuration. At this point, the primary minimum switches from $\theta_r = 0°$ to $\theta_r = 90°$, and the system in principle undergoes a first-order (i.e. discontinuous) transition from the tip-to-tip state to the

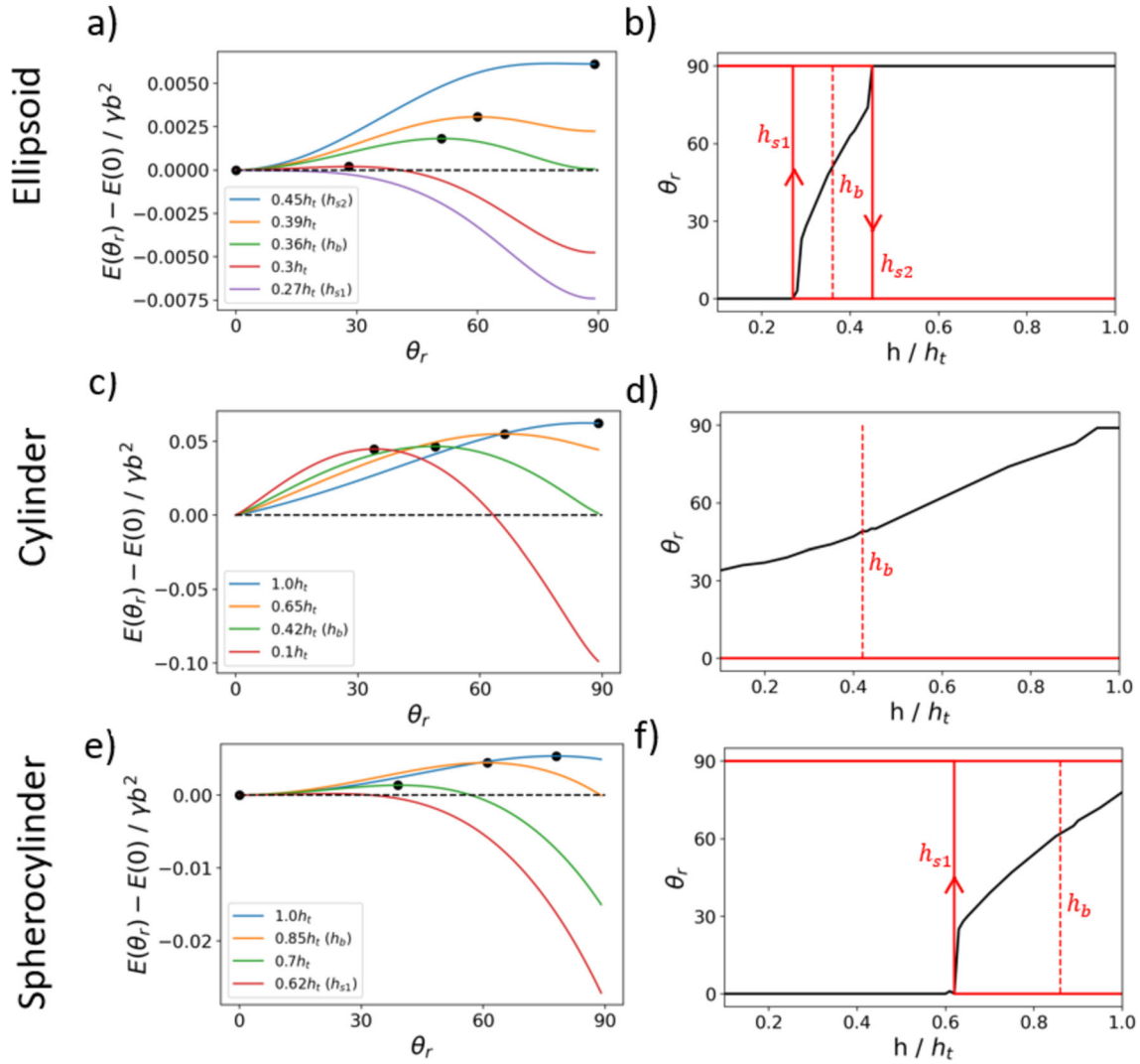

Fig. 9 **a**, **c**, **e** Interfacial energy curves for two particles in contact as a function of the roll-over angle θ_r (relative to the energy at $\theta_r = 0°$) for different drop heights around the roll-over transition for **a** ellipsoids with $\theta_w = 110°$, **c** cylinders with $\theta_w = 70°$, **e** spherocylinders with $\theta_w = 70°$. The filled black circles represent the maxima for each curve. **b**, **d**, **f** Locally stable values of θ_r as a function of h (red curve) and the value of θ_r corresponding to the energy barrier maxima as a function of h (black curve) for **b** ellipsoids with $\theta_w = 110°$, **d** cylinders with $\theta_w = 70°$, **f** spherocylinders with $\theta_w = 70°$. The vertical dashed curve denotes the thermodynamic roll-over transition at the binodal point $h = h_b$, while the vertical arrows pointing up or down denote the actual roll-over transitions that occur at the spinodal points $h = h_{s1}$, h_{s2}

side-to-side state. The height h_b therefore corresponds to the binodal point of the roll-over transition. However, in practice, because the energy barrier between the two minima is typically much larger that $k_B T$, even for rods on the nanoscale, there is significant hysteresis in the roll-over transition. Specifically, for decreasing h, the system only undergoes an irreversible transition from the tip-to-tip state to the side-to-side state when $h = h_{s1} = 0.27b$ (purple curve), where the maxima of the energy barrier shift to $\theta_r = 0°$ and the local minimum at $\theta_r = 0°$ disappear. On the other hand, for increasing h, the system only undergoes an irreversible transition from the side-to-side state to the tip-to-tip state when $h = h_{s2} = 0.45b$ (blue curve), where the maxima of the energy barrier shift to $\theta_r = 90°$ and the local minimum at $\theta_r = 90°$ disappears. The heights h_{s1}, h_{s2} therefore correspond to the spinodal points of the roll-over transition.

The key features of the roll-over transition for hydrophobic ellipsoids are summarised in Fig. 9b where we plot the locally stable values of θ_r as a function of h (red curve) and the value of θ_r corresponding to the energy barrier maxima as a function of h (black curve). We see that at large h, the system is initially in the tip-to-tip state $\theta_r = 0°$. As we decrease h to the binodal point h_b, thermodynamically the system will undergo a first-order

transition from the tip-to-tip state to the side-to-side state (dashed vertical line). However, as discussed earlier, in practice, it is only when we decrease h to the spinodal point h_{s1} that the system undergoes an irreversible transition from the tip-to-tip state to the side-to-side state (solid vertical line pointing up). Similarly, when the system is initially in the side-to-side state $\theta_r = 90°$ at low values of h, it is only when we increase h to the spinodal point h_{s2} that the system undergoes an irreversible transition from the side-to-side state to the tip-to-tip state (solid vertical line pointing down). Note that the spinodal points h_{s1} and h_{s2} are the values of h where the energy maxima curve (black curve) first meet $\theta_r = 0°$ and $\theta_r = 90°$, respectively. Note also that points to the right of the binodal point on the bottom branch of the red curve and to the left of the binodal point on the top branch of the red curve are equilibrium states, while all other points on the red curve are metastable states.

In Fig. 9c, we plot the interfacial energy (relative to the value at $\theta_r = 0°$) as a function of θ_r for hydrophilic cylinders for different drop heights h. Once again, we see that at large h (e.g. the blue curve), there is a single minimum corresponding to the tip-to-tip configuration, but as we decrease h, the energy curve develops a local minimum at $\theta_r = 90°$ which is separated from the primary minimum at $\theta_r = 0°$ by an energy barrier. As h is decreased further to the binodal point $h_b = 0.42b$ (green curve), the energy of the side-to-side configuration becomes equal to that of the tip-to-tip configuration and thermodynamically, the system should undergo a first-order transition from the tip-to-tip state to the side-to-side state at this point. However, this transition does not occur in practice because the energy barrier between the two minima is generally too large. Interestingly, for cylinders, the local minima at $\theta_r = 0°$ do not disappear, or equivalently the maximum of the energy barrier does not shift to $\theta_r = 0°$, even at the lowest drop height we studied at $h = 0.1h_t$ (red curve). This means that cylinders effectively do not have a lower spinodal point h_{s1} so that they do not undergo a roll-over transition from the tip-to-tip state to the side-to-side state even for small h. Interestingly, cylinders adsorbed at flat interfaces also do not undergo a roll-over transition because they are prevented from doing so by the capillary 'hinges' between contacting cylinders created by the sharp edges of the cylinders [22]. The significant and persistent energy barrier we see in Fig. 9c is presumably due to the same effect. The key features of the roll-over transition for hydrophilic cylinders discussed above are summarised in Fig. 9d where all the lines have the same meaning as in Fig. 9b.

Finally, in Fig. 9e we plot the interfacial energy (relative to the value at $\theta_r = 0°$) as a function of θ_r for hydrophilic spherocylinders for different drop heights h. Interestingly, we see that even at $h = h_t$ (blue curve), while the primary minimum is at $\theta_r = 0°$, there is already a local minimum at $\theta_r = 90°$, suggesting that spherocylinders do not have an upper spinodal point h_{s2}. As h is decreased to the binodal point $h_b = 0.85b$ (orange curve), the energy of the side-to-side configuration becomes equal to that of the tip-to-tip configuration. Thermodynamically, the system undergoes a first-order transition from the tip-to-tip state to the side-to-side state at this point, but in practice this transition only occurs when we decrease h further to the lower spinodal point $h_{s1} = 0.62b$, where the maxima of the energy barrier shift to $\theta_r = 0°$ and the local minimum at $\theta_r = 0°$ disappears. The key features of the roll-over transition for hydrophilic spherocylinders discussed above are summarised in Fig. 9f where all lines have the same meaning as in Fig. 9b.

We note that the effective roll-over transition height h_{s1} is significantly greater for spherocylinders ($h_{s1} \approx 0.62h_t$) compared to ellipsoids ($h_{s1} \approx 0.27h_t$) and cylinders ($h_{s1} \approx 0$). Since the strong lateral spatial confinement needed to align the rods into the tip-to-tip configuration requires us to work in the immersion regime $h < h_t$, this means that it is easier to use our capillary assembly method to prepare tip-to-tip assemblies of ellipsoids and cylinders compared to spherocylinders because the drop height window over which we can prepare tip-to-tip assemblies ($h_{s1} < h < h_t$) is much wider for the former compared to the latter. Finally, we note that the results in this section provide insights into how the structure of clusters of rods adsorbed at cylindrical drops evolves during the drying of the droplet.

4 Conclusions

We have used the finite element method Surface Evolver to study the capillary assembly of rod-shaped particles adsorbed at a sessile liquid drop with cylindrical geometry. Specifically, we considered the immersion regime where the drop height is less than the radius of the rods and the lateral width of the cylindrical drop is much greater than the length of the rods, and we studied the configuration of single and multiple rods as a function of drop height, particle shape (ellipsoid, cylinder, spherocylinder) and contact angle.

We found that for low enough drop heights, regardless of the shape or contact angle of the rods, all rods orientate themselves parallel to the long axis of the cylindrical drop and are strongly confined laterally to be at

the centreline of the cylindrical drop. We also found that the rods experience strong and long-range immersion capillary forces which assemble the rods tip-to-tip at larger drop heights and, in the case of ellipsoids and spherocylinders, side-to-side when we reduce the drop height, for example through drying. We note that the capillary forces discussed above are very strong, allowing us to order rods even on the nanoscale.

The fact that we can control the self-assembly of rods using cylindrical drops whose lateral dimensions are much greater than the length of the rods allows us, for example, to control the configuration of nanorods using near micron-scale droplets, greatly simplifying the task of fabricating the liquid templates required to realise this assembly method. Our capillary assembly method therefore provides a facile method for organising micro- and nanoscale objects into complex cluster structures and we hope that our study will stimulate future experiments in this direction.

Acknowledgements This project has received funding from the European Union's Horizon 2020 research and innovation programme under grant agreement No 861950, project POSEIDON. JE and DMAB acknowledge the Viper High Performance Computing facility of the University of Hull and its support team.

Author contributions JE performed all theoretical modelling; JE and DMAB wrote the manuscript; all other authors commented on the manuscript; DMAB supervised the study; DMAB and TSH conceptualised the study.

Funding H2020 Future and Emerging Technologies, 861950, Jack L. Eatson, 861950, Jacob R. Gordon, 861950, Tommy S. Horozov, 861950, Martin Buzza.

Declarations

Conflicts of interest There are no conflicts to declare.

References

1. Aveyard, R., Binks, B.P., Clint, J.H.: Emulsions stabilised solely by colloidal particles. Adv. Colloid Interface Sci. **100–102**, 503–546 (2003)
2. Binks, B.P., Horozov, T.S.: Colloidal particles at liquid interfaces. Cambridge University Press, Cambridge (2006). https://doi.org/10.1017/CBO9780511536670
3. Dinsmore, A.D., et al.: Colloidosomes: selectively permeable capsules composed of colloidal particles. Science **298**, 1006–1009 (2002)
4. Dickinson, E.: Food emulsions and foams: stabilization by particles. Curr. Opin. Colloid Interface Sci. **15**, 40–49 (2010)
5. Forth, J., et al.: Building reconfigurable devices using complex liquid-fluid interfaces. Adv. Mater. **31**, 1–39 (2019)
6. Rey, M., Law, A.D., Buzza, D.M.A., Vogel, N.: Anisotropic self-assembly from isotropic colloidal building blocks. J. Am. Chem. Soc. **139**, 17464–17473 (2017)
7. Menath, J., et al.: Defined core–shell particles as the key to complex interfacial self-assembly. Proc. Natl. Acad. Sci. **118**, 1–10 (2021)
8. Pieranski, P.: Two-dimensional interfacial colloidal crystals. Phys. Rev. Lett. **45**, 569–572 (1980)
9. Law, A.D., Buzza, D.M.A., Horozov, T.S.: Two-dimensional colloidal alloys. Phys. Rev. Lett. **106**, 1–4 (2011)
10. Law, A.D., Auriol, M., Smith, D., Horozov, T.S., Buzza, D.M.A.: Self-assembly of two-dimensional colloidal clusters by tuning the hydrophobicity, composition, and packing geometry. Phys. Rev. Lett. **110**, 1–5 (2013)
11. Kralchevsky, P.A., Nagayama, K.: Capillary interactions between particles bound to interfaces, liquid films and biomembranes. Adv. Colloid Interface Sci. **85**, 145–192 (2000)
12. Kralchevsky, P.A., Nagayama, K.: Capillary forces between colloidal particles. Langmuir **10**, 23–36 (1994)
13. Botto, L., Lewandowski, E.P., Cavallaro, M., Stebe, K.J.: Capillary interactions between anisotropic particles. Soft Matter **8**, 9957–9971 (2012)
14. Davies, G.B., Krüger, T., Coveney, P.V., Harting, J.: Detachment energies of spheroidal particles from fluid-fluid interfaces. J. Chem. Phys. **141**, 154902 (2014)
15. Dasgupta, S., Auth, T., Gompper, G.: Nano- and microparticles at fluid and biological interfaces. J. Phys. Condens. Matter **29**, 373003 (2017)

16. Nicolson, M.M.: The interaction between floating particles. Math. Proc. Cambridge Philos. Soc. **45**, 288–295 (1949)
17. Loudet, J.C., Yodh, A.G., Pouligny, B.: Wetting and contact lines of micrometer-sized ellipsoids. Phys. Rev. Lett. **97**, 1–4 (2006)
18. Lehle, H., Noruzifar, E., Oettel, M.: Ellipsoidal particles at fluid interfaces. Eur. Phys. J. E **26**, 151–160 (2008)
19. Lewandowski, E.P., et al.: Orientation and self-assembly of cylindrical particles by anisotropic capillary interactions. Langmuir **26**, 15142–15154 (2010)
20. Loudet, J.C., Alsayed, A.M., Zhang, J., Yodh, A.G.: Capillary interactions between anisotropic colloidal particles. Phys. Rev. Lett. **94**, 2–5 (2005)
21. Zhang, Z., Pfleiderer, P., Schofield, A.B., Clasen, C., Vermant, J.: Synthesis and directed self-assembly of patterned anisometric polymeric particles. J. Am. Chem. Soc. **133**, 392–395 (2011)
22. Botto, L., Yao, L., Leheny, R.L., Stebe, K.J.: Capillary bond between rod-like particles and the micromechanics of particle-laden interfaces. Soft Matter **8**, 4971–4979 (2012)
23. Dushkin, C.D., Kralchevsky, P.A., Paunov, V.N., Yoshimura, H., Nagayama, K.: Torsion balance for measurement of capillary immersion forces. Langmuir **12**, 641–651 (1996)
24. Ershov, D., Sprakel, J., Appel, J., Stuart, M.A.C., Van Der Gucht, J.: Capillarity-induced ordering of spherical colloids on an interface with anisotropic curvature. Proc. Natl. Acad. Sci. U. S. A. **110**, 9220–9224 (2013)
25. Würger, A.: Curvature-induced capillary interaction of spherical particles at a liquid interface. Phys. Rev. E—Stat Nonlinear Soft Matter Phys. **74**, 1–9 (2006)
26. Blanc, C., et al.: Capillary force on a micrometric sphere trapped at a fluid interface exhibiting arbitrary curvature gradients. Phys. Rev. Lett. **111**, 058302 (2013)
27. Domínguez, A., Oettel, M., Dietrich, S.: Force balance of particles trapped at fluid interfaces. J. Chem. Phys. (2008). https://doi.org/10.1063/1.2890035
28. Lewandowski, E.P., Bernate, J.A., Searson, P.C., Stebe, K.J.: Rotation and alignment of anisotropic particles on nonplanar interfaces. Langmuir **24**, 9302–9307 (2008)
29. Cavallaro, M., Botto, L., Lewandowski, E.P., Wang, M., Stebe, K.J.: Curvature-driven capillary migration and assembly of rod-like particles. Proc. Natl. Acad. Sci. USA **108**, 20923–20928 (2011)
30. Hu, D.L., Bush, J.W.M.: Meniscus-climbing insects. Nature **437**, 733–736 (2005)
31. Yu, Y., Guo, M., Li, X., Zheng, Q.S.: Meniscus-climbing behavior and its minimum free-energy mechanism. Langmuir **23**, 10546–10550 (2007)
32. Eatson, J.L., et al.: Capillary assembly of anisotropic particles at cylindrical fluid-fluid interfaces. Langmuir **39**, 6006–6017 (2023)
33. Brakke, K.A.: The surface evolver. Exp. Math. **1**, 141–165 (1992)
34. Newton, B.J., Buzza, D.M.A.: Magnetic cylindrical colloids at liquid interfaces exhibit non-volatile switching of their orientation in an external field. Soft Matter **12**, 5285–5296 (2016)
35. Newton, B.J., Brakke, K.A., Buzza, D.M.A.: Influence of magnetic field on the orientation of anisotropic magnetic particles at liquid interfaces. Phys. Chem. Chem. Phys. **16**, 26051–26058 (2014)
36. Coertjens, S., Moldenaers, P., Vermant, J., Isa, L.: Contact angles of microellipsoids at fluid interfaces. Langmuir **30**, 4289–4300 (2014)
37. Newton, B.J., Mohammed, R., Davies, G.B., Botto, L., Buzza, D.M.A.: Capillary interaction and self-assembly of tilted magnetic ellipsoidal particles at liquid interfaces. ACS Omega **3**, 14962–14972 (2018)
38. Morgan, S.O., Fox, J., Lowe, C., Adawi, A.M., Bouillard, J.-S.G., Stasiuk, G.J., Horozov, T.S., Buzza, D.M.A.: Adsorption trajectories of nonspherical particles at liquid interfaces. Phys. Rev. E **103**, 042604 (2021)
39. Blake, T.D.: The physics of moving wetting lines. J. Colloid Interface Sci. **299**, 1 (2006)
40. Guzowski, J., Tasinkevych, M., Dietrich, S.: Free energy of colloidal particles at the surface of sessile drops. Eur. Phys. J. E **33**, 219–242 (2010)
41. Guzowski, J., Tasinkevych, M., Dietrich, S.: Effective interactions and equilibrium configurations of colloidal particles on a sessile droplet. Soft Matter **7**, 4189–4197 (2011)